

Gravity-destabilized nonwetting phase invasion in macroheterogeneous porous media: Near-pore-scale macro modified invasion percolation simulation of experiments

Robert J. Glass, Stephen H. Conrad, and Lane Yarrington

Flow Visualization and Processes Laboratory, Sandia National Laboratories, Albuquerque, New Mexico

Abstract. We reconceptualize “macro” modified invasion percolation (MMIP) at the near pore (NP) scale and apply it to simulate the nonwetting phase invasion experiments of *Glass et al.* [2000] conducted in macroheterogeneous porous media. For experiments where viscous forces were nonnegligible, we redefine the total pore filling pressure to include viscous losses within the invading phase as well as the viscous influence to decrease randomness imposed by capillary forces at the front. NP MMIP exhibits the complex invasion order seen experimentally with characteristic alternations between periods of gravity-stabilized and destabilized invasion growth controlled by capillary barriers. The breaching of these barriers and subsequent pore-scale fingering of the nonwetting phase is represented extremely well, as is the saturation field evolution and total volume invaded.

1. Introduction

Recent experiments presented by *Glass et al.* [2000], henceforth referred to as GCP, have demonstrated the complexity of the gravity-destabilized nonwetting invasion process in macroheterogeneous porous media and suggested the difficulty of attempting simulation using standard porous continuum approaches. These experiments show a characteristic alternation between gravity-stabilized and destabilized invasion growth controlled by the sequential capillary barriers (CBs) within the heterogeneous field. The final nonwetting invasion structure existed as a set of macroscopic pools connected by pore-scale fingers. Viscous forces were shown to increase the number of fingers, their width, and the height of pools above CBs. The experiments also documented unsteady pulsation behind the invasion front; however, the pulsation did not significantly influence the maximum extent of the invasion structure.

In an accompanying analysis, GCP also developed length scales that describe pool height, finger width, and pulsation. Each of these length scales required conceptualization at the pore scale to predict experimental behavior. To avoid the problems of porous continuum simulation, a “structural” growth model was proposed at the macroscale that would assemble these length scales to build the nonwetting phase migration pathway directly, its geometry of fingers and pools, and the locations of pulsation within a complex heterogeneous formation. Such an approach is underpinned by the physics of the pore-scale behavior and is a more abstracted or upscaled version of macromodified invasion percolation (MMIP) developed and applied originally by *Glass et al.* [1993, 1995] to the gravity-destabilized, dense nonaqueous phase liquid (DNAPL) migration problem.

The development of such modeling approaches is in its infancy compared to conventional porous continuum conceptu-

alizations of reality. Here we continue to lay a foundation for MMIP by first reconceptualizing it generally in a form that encompasses the near pore (NP) scale and then comparing NP MMIP simulations to the laboratory experiments presented by GCP. Our initial NP MMIP simulations of the experiments show several discrepancies which lead to modifications for small capillary property mismatches and the inclusion of viscous effects. Once these modifications are accomplished, we find that NP MMIP can model the complex experimental invasion sequence and saturation field evolution exceptionally well, both when viscous forces are negligible and when they are not.

2. MMIP and NP MMIP Model Conceptualization

MMIP bases its properties for spanning a grid block of porous media (the macroscale) on the smaller-scale pore network behavior seen in standard invasion percolation (IP) simulations [e.g., *Wilkinson and Willemsen*, 1983] and pore network micromodel experiments [e.g., *Lenormand and Zaccaro*, 1985]. We note that this approach has also been suggested by *Kueper and McWorter* [1992] and *Ioannidis et al.* [1996] for gravity-stabilized conditions. In isotropic, random pore networks with no spatial correlation, as an invading fluid displaces a defending fluid in the absence of gravity, a threshold radius is achieved after which the network is spanned, or “percolates,” in all directions. The radius at this percolation threshold is used in the macromodel to represent a “spanning” radius R for the block. The pressure difference between invading and defending phases, or capillary pressure P_c , required to achieve the spanning radius is given by

$$P_c = \frac{-2\sigma \cos(\alpha)}{R}, \quad (1)$$

where σ is the interfacial tension and α is the effective contact angle within the fluid/fluid/solid system (measured through the invading phase with α between 0° and 90° for wetting and 90°

This paper is not subject to U.S. copyright. Published in 2001 by the American Geophysical Union.

Paper number 2000WR900294.

and 180° for nonwetting invasion). Gravity forces are represented by the pressure differential P_g :

$$P_g = \Delta\rho gz, \quad (2)$$

where $\Delta\rho$ is the density difference between the two fluids ($\rho_{\text{defender}} - \rho_{\text{invader}}$), z is the distance into the network, and g is the component of the acceleration due to gravity in the direction of z (i.e., $g = -g$ for upward invasion). For gravity-destabilized invasion, P_g becomes more negative as the phase advances into the network. The total invasion pressure for a block P_t is simply given by the sum of P_c and P_g :

$$P_t = \frac{-2\sigma \cos(\alpha)}{R} + \Delta\rho gz. \quad (3)$$

Implementation of MMIP requires the problem domain to be discretized into a grid (two- or three-dimensional) with a chosen connectivity and R values assigned to each grid block. An IP algorithm [e.g., *Wilkinson and Willemsen*, 1983] is then applied on the P_t field to determine the growth pattern in time as invading fluid is added at the injection point. An IP algorithm simply selects the block connected to the growing cluster that has the lowest total invasion pressure as calculated using (3) and invades it. When a block is invaded, the list of blocks connected to the growing cluster is modified and sorted, the next block with the lowest invasion pressure is selected, invaded, and so on. Thus, at each growth step, only a single block is added to the invaded structure.

Because in MMIP we do not consider the details of individual “throats” and “pores” but rather the behavior of a subnetwork of these features, R represents the critical “throat” or critical “pore” within the block for nonwetting or wetting fluid invasion, respectively. We can also apply this conceptual model at the “near pore scale” where a block contains a small void space “network” that is characterized by local spanning radii for wetting and nonwetting invasion. For this NP MMIP conceptualization we can obtain R values for blocks composing the material of interest directly from its measured capillary pressure-saturation curves. For nonwetting invasion we take the primary drainage curve, normalize saturation by $(1 - S_{wr})$, where S_{wr} is the wetting fluid residual value, and then transform capillary pressure to effective R using (1) to yield a cumulative probability distribution function (CDF) for R that characterizes the material of interest. The R for each block composing this material is then chosen from this distribution. S_{wr} for the near pore scale represents wetting phase that is contained in films, pendular rings between grains, and trapped pores within the void space. At this scale, trapping of the defending phase could be considered directly when a block is surrounded by other blocks. In our application here we will not consider such block-scale trapping directly but will represent this process in the residual value.

NP MMIP has many advantages over traditional forms of IP where the conceptual model is tied to balls and sticks or even more complicated throat and pore geometries [e.g., *Reeves and Celia*, 1996]. Such geometries are difficult to justify topologically in granular porous media and could actually lead to a divergence between model results and data. Instead, we make use of easily measured pressure-saturation curves directly with an appropriate volume-averaged conceptual model. This also contrasts with the standard continuum approach based on a traditional representative elementary volume; we do not require that the property be “uniform” for a given material and

instead capture its near-pore-scale stochastic nature within the R field.

Application of NP MMIP requires discretizing the problem into a network of blocks and specifying a connectivity between blocks. For simplicity, we work with discretizations that divide the domain into a grid of cubes. At the NP scale the mean grain size is representative of the average spacing between pores and so represents a reasonable lower limit for grid block size. The mean grain size may vary from unit to unit. Results are relatively insensitive to the scale of discretization above the mean grain size until the block size becomes of the order of the variation in capillary potential within a unit. When this happens, gravity begins to artificially overwhelm capillary forces within a particular unit. This issue requires additional study with respect to upscaling but is less important in our current NP conceptualization and application here.

Connectivity influences the invasion structure by controlling the subset of blocks that are available for filling. The larger the connectivity, the larger the population sampled and the higher the probability of finding blocks with a lower spanning pressure. In this study we constrain ourselves to connectivities of 4 (orthogonal) and 8 (orthogonal plus diagonal) in two dimensions and 6 (orthogonal) and 26 (orthogonal plus diagonal) in three dimensions. Within a gravity field the connectivity also influences the relative weighting of horizontal to vertical invasion. Orienting down the gravitational potential gradient, a connectivity of 4 in two dimensions has two horizontal blocks, one downstream and one upstream; a connectivity of 8 in two dimensions has two horizontal blocks, three downstream and three upstream; a connectivity of 6 in three dimensions has four horizontal blocks, one downstream and one upstream; and a connectivity of 26 in three dimensions has eight horizontal blocks, nine downstream and nine upstream. This connectivity biases growth within a gravity field because greater/lesser access to pores in a given direction will lead to a higher/lower probability of growth in that direction. Thus slightly narrower fingers are simulated in three-dimensional (3-D) networks and when both orthogonal and diagonal blocks are accessible.

Additional processes that influence P_t can be easily added within the NP MMIP model. First- and higher-order viscous effects will be discussed in section 3 in comparison to the experiment. Other modifications such as the influence of macroscopic interfacial curvature, local saturation-dependent viscous forces, or variability in time and space of the contact angle can also be incorporated as can simultaneous drainage and wetting such as seen in experiments that exhibit pulsation. However, we will not discuss these additional modifications further here.

3. Comparison of NP MMIP to Experiment

Experiments reported by GCP were designed and conducted within a thin (1 cm) but extensive (26 cm wide and 60 cm tall) sand chamber filled with translucent sands such that saturation and invasion order integrated over the thickness of the chamber could be monitored in time using quantitative light transmission visualization techniques. The heterogeneous sand structure (heterostructure) was composed of a series of capillary barriers (CBs) reminiscent of fluvial channel lag cut-and-fill architecture created with three sand units: coarse, medium, and fine (sand properties given in Table 1). Gravity-destabilized, nonwetting phase invasion experiments were con-

ducted where the interfacial tension, density difference, and viscosity were varied between two fluid-fluid systems: CO₂-water and trichloroethylene (TCE)-water (fluid properties given in Table 2). The nonwetting fluid was injected into the water-saturated heterostructure near the middle of one end, and the invasion process was recorded in a series of high-resolution digital images (taken every ~ 0.33 mL of injected fluid) until the nonwetting phase reached the far side of the chamber. Digital images were processed to provide quantitative saturation fields (pixel size 0.4495 mm by 0.4495 mm across the entire experimental field) that clearly showed the pore-scale nature of the invasion process.

Here we consider only the CO₂ and TCE experiments that were conducted in the same sand pack (the “primary” heterostructure, Figure 1a of GCP) where CO₂ was initially injected from below, CO₂ dissolved away, the chamber was inverted, and finally TCE was injected from above. Considering fluid properties alone (see Table 2), we see that CO₂ has slightly higher σ and $\Delta\rho$ than TCE (factor of 2–3). Additionally, because flow rates for these two invasion experiments were nearly the same (1.2 mL/min for CO₂ and 0.90 mL/min for TCE), viscous forces relative to capillary and gravity forces were substantially different because of the ~ 40 times greater viscosity of TCE relative to CO₂. Analysis of results presented by GCP suggested that while viscous forces were negligible for the CO₂ system, they were nonnegligible for the TCE-water experiments. Thus, by considering these experiments conducted in the same heterostructure, we can assess NP MMIP where the development in section 2 applies and then consider modifications to the model for viscous effects in context of the data.

In the following we first describe our problem definition and simulation processing procedures. We then present a set of initial simulations and compare to the experimental results. We follow with a set of modified simulations that first correct for capillary property discrepancies and then include first- and second-order viscous influences. Finally, we evaluate the saturation fields simulated by NP MMIP in light of the experiments.

3.1. Problem Definition and Simulation Processing

We translated the experimental heterostructure into a field of effective spanning radius values by first dividing the digital image of the sand pack (580×1236 pixels) into the individual sand types using pixel intensity (the coarser the unit, the more light passes). Edges of units were then resolved by eye where digital methods failed because of light scatter. The image was then rescaled to yield the template “unit” network with block size equal to the mean grain size of the coarse unit (240×511 pixels, 0.1087^2 cm²/pixel). For 3-D networks, the two-dimensional (2-D) unit field was “extruded” to the thickness of the experiment (nine blocks). Each block in the resulting unit network was then randomly assigned an individual R value

Table 1. Sand Properties^a

Grain Size	Sieve Size	k , cm ²	Mean Grain, mm	Porosity
Coarse	12–20	6.32E-06 ^b	1.087 ± 0.001	0.35
Medium	30–40	1.20E-06	0.488 ± 0.003	0.35
Fine	50–70	2.97E-07	0.259 ± 0.001	0.36

^aSource is GCP.

^bRead 6.32E-06 as 6.32×10^{-6} .

Table 2. Fluid Properties^a

Chemical	Density, g/mL	Interfacial Tension, dyn/cm	Viscosity poise
CO ₂	0.002	71.40 ± 0.85	1.48E-04 ^b
H ₂ O	0.996	NA ^c	1.00E-02
TCE	1.464	26.90 ± 0.63	5.76E-03

^aSource is GCP.

^bRead 1.48E-04 as 1.48×10^{-4} .

^cNA is not applicable.

using CDFs built from the measured primary drainage pressure-saturation curves for each unit as described above. Within each unit we assumed no spatial correlation when assigning R . Contact angle α was taken as 180° for invasion of either CO₂ or TCE.

The heterostructure and a representative pore radius field are shown in Figures 1a and 1b. As a simple check on our NP MMIP formulation and assignment method for R field distributions, we conducted gravity-stabilized air invasion simulations of the experiments used to measure the primary drainage pressure-saturation curves. Comparison of the final equilibrium (hydrostatic) profiles is shown in Figure 1c. As we would expect, the results are nearly identical. Small differences occur only near the nonwetting entry value where simulations are slightly more abrupt than the experimental data suggest.

To compare with experimental invasion data, composite 2-D order images are compiled by tracking the first invasion at a location across the thickness of the 3-D network just as our image analysis of the sequential saturation fields did (GCP) to develop similar order images from the experimental data. Additionally, 2-D saturation fields are calculated from the 3-D network results by averaging across the thickness of the network. Images in all figures and plates are oriented such that flow is in the same direction to facilitate comparison; that is, the CO₂ invasion is rotated 180° with gravity now acting upward in the image. Invaded volumes were calculated by multiplying the volume of invaded blocks by the product of $(1 - S_{wr})$ and the porosity, taken for the coarse sand as 0.83 and 0.35, respectively.

3.2. Initial Simulations

A full suite of CO₂ and TCE invasion simulations using (3) was conducted on both 2-D (connectivities 4 and 8) and 3-D (connectivities 6 and 26) networks using 10 different realizations of each R field. Comparison across the different realizations shows some variability with slight differences in pool height, finger location, and final invaded volume at breakthrough. Additionally, directional bias inherent in the choice of network dimensionality and connectivity slightly influences the details of finger structure and saturation. For the sake of brevity, we choose to present only the 3-D orthogonal results (connectivity 6) as they most closely match the data. Table 3 reports data associated with the full set of 10 simulations, and Plates 1–3 and Figures 2 and 3 are shown for a single R field realization.

Composite order images shown in Plate 1 show a strong qualitative similarity to the experimental images. At breakthrough the field is composed of a series of macroscopic pools connected by pore-scale fingers. The breaching of CBs also is pore-scale (i.e., fingers) as we found in the experiments. How-

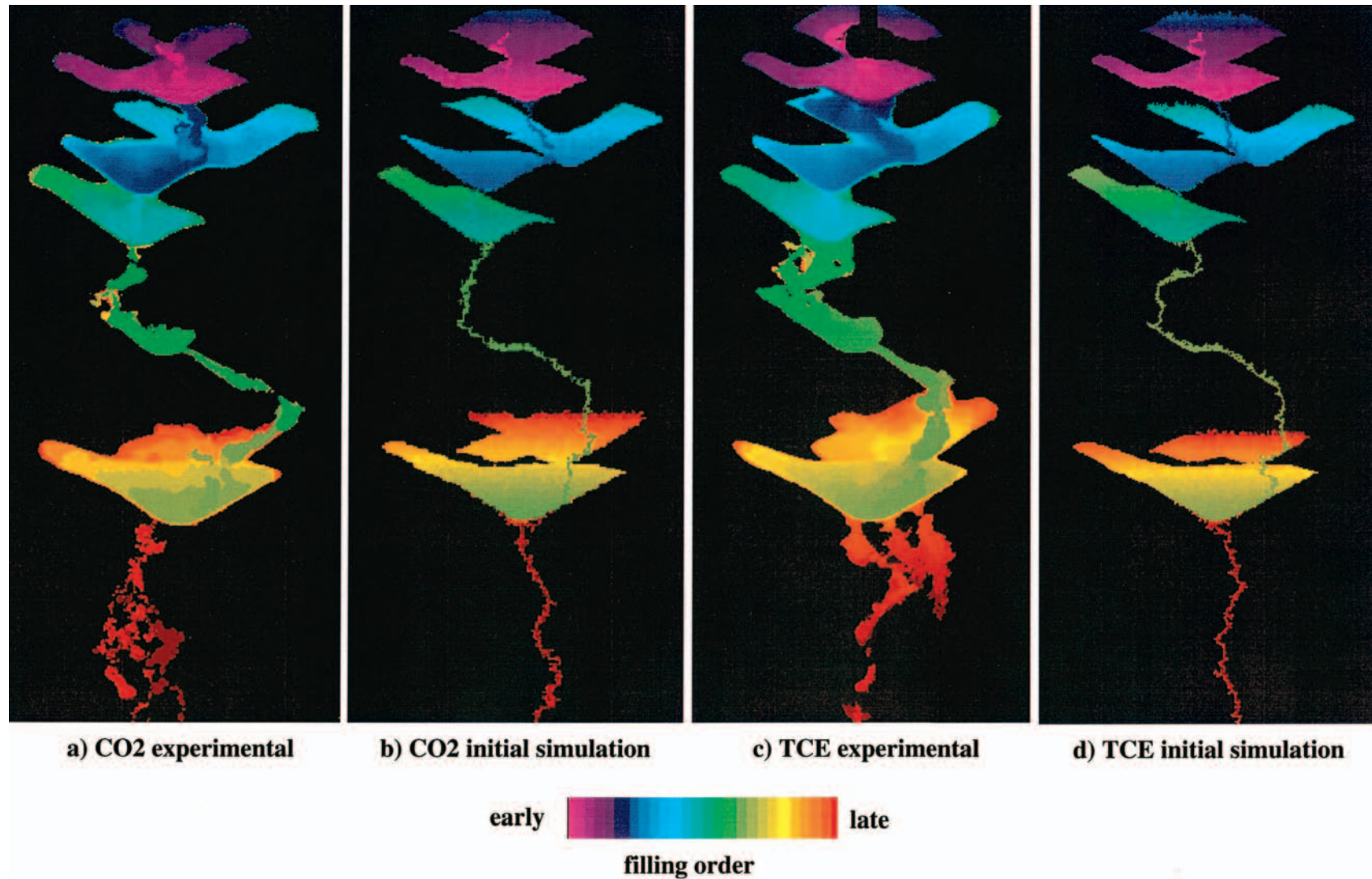


Plate 1. Experimental invasion order images and initial 3-D near-pore-scale macromodified invasion percolation (NP MMIP) simulations: (a) CO₂ experiment, (b) CO₂ NP MMIP simulation, (c) TCE experiment, and (d) trichloroethylene (TCE) NP MMIP simulation. Colors represent first arrival filling order integrated across the thickness of the chamber or simulation network.

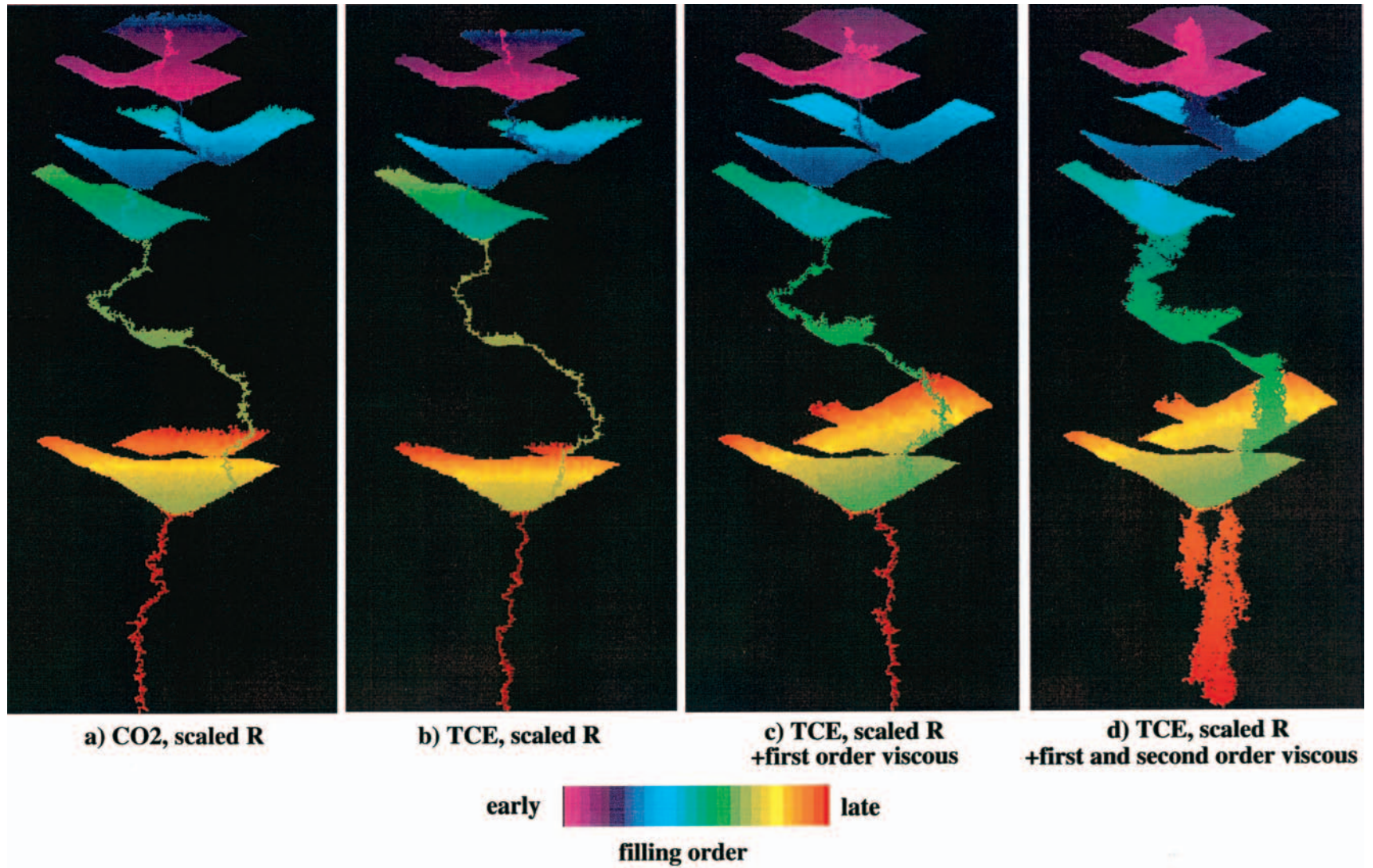


Plate 2. Modified 3-D NP MMIP simulations: (a) CO₂ on scaled R field, (b) TCE on scaled R field, (c) TCE on scaled R field with first-order viscous forces included, (d) TCE on scaled R field with first- and second-order viscous forces included (60 blocks per step). Colors represent first arrival filling order integrated across the thickness of the chamber or simulation network.

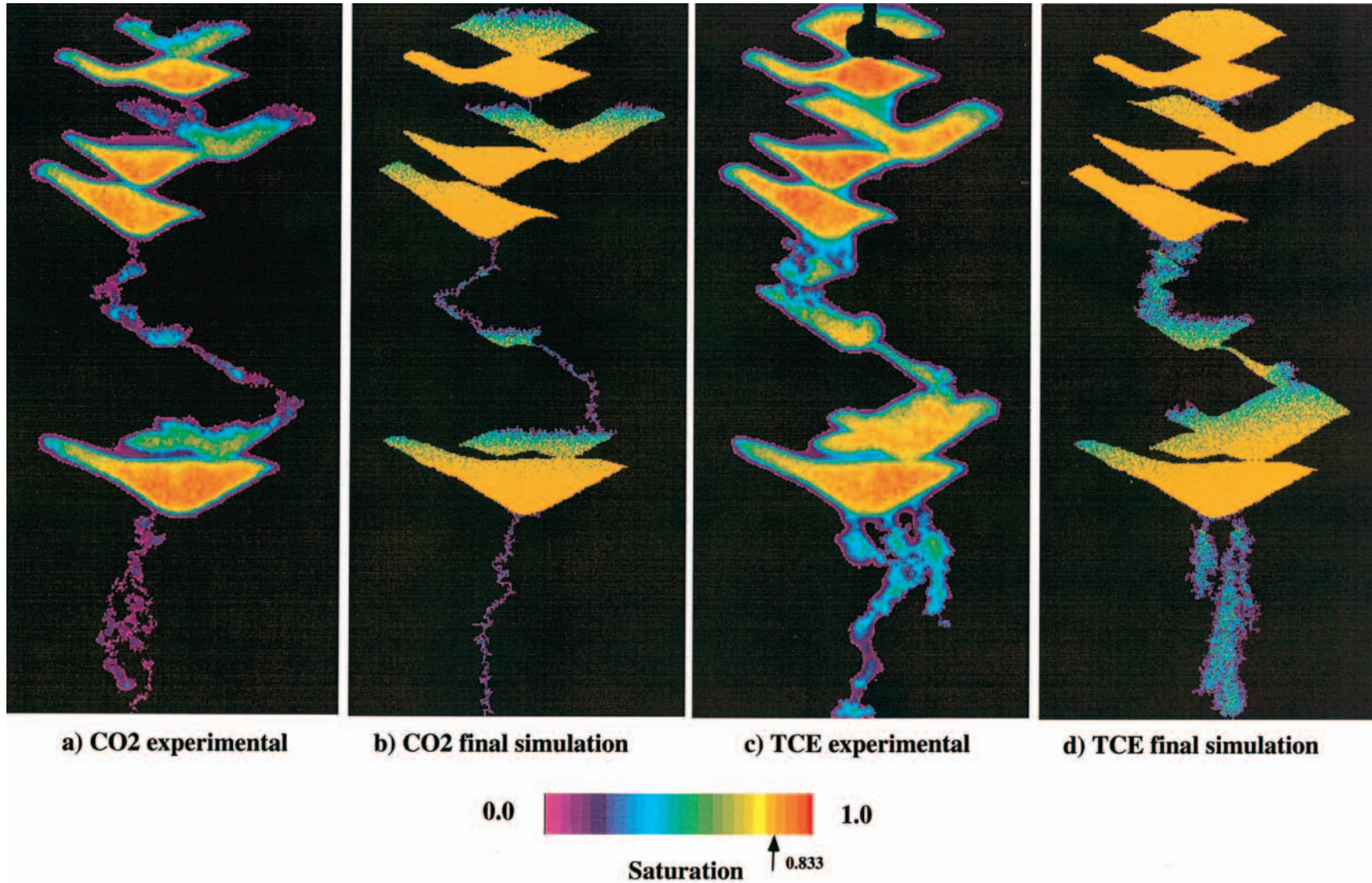


Plate 3. Thickness-integrated saturation fields at system breakthrough: (a) CO₂ experiment, (b) CO₂ NP MMIP simulation on scaled R field, (c) TCE experiment, (d) TCE NP MMIP simulation on scaled R field with first- and second-order viscous forces included (60 blocks per step). Colors represent nonwetting saturation averaged across the thickness of the chamber or simulation network; nonwetting residual saturation ($1 - S_{wr}$) of 0.83 is noted on the color bar. The variability seen in the experiment reflects both pore-scale variability and error in the method due to light scatter when the phase does not fully span the chamber thickness such as in finger zones, as well as around the edges of pools. Note that the simulation incorporates the average value of the saturation within each block ($1 - S_{wr}$), and so when the phase spans the thickness of the simulation network within the pools, variability such as seen in the experiment is averaged out.

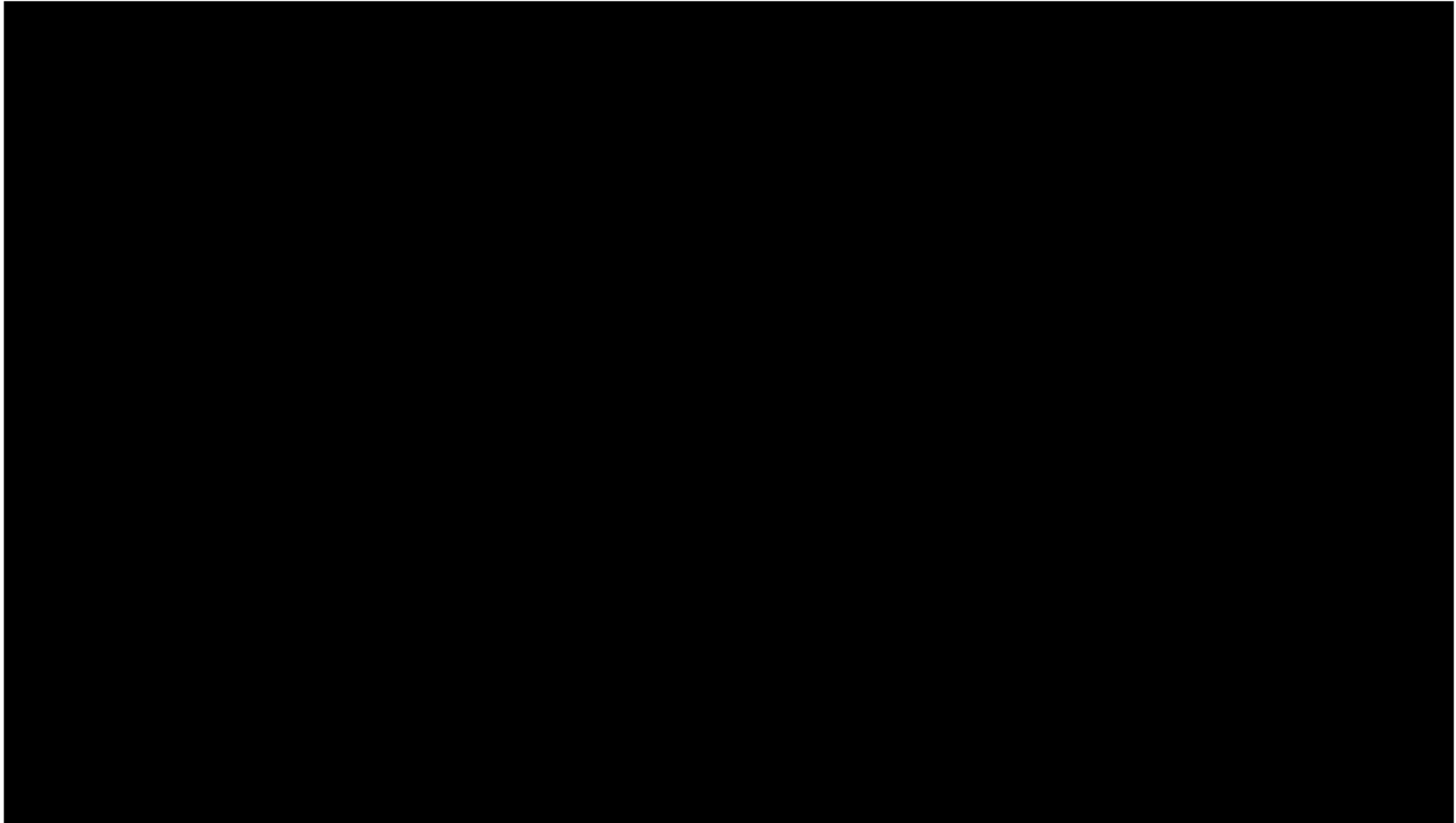


Figure 1. Simulation of R field and unit drainage curves: (a) Digital image of the heterogeneous sand pack used in the invasion experiments. In Figure 1a the coarse sand transmits the most light and hence is the lightest; the medium sand appears gray; and the fine sand appears dark. The injection port and four major capillary barriers (labeled CB1 through CB4) are identified. These capillary barriers occur where medium sand separates coarse sand units. (b) Representative 2-D slice through a 3-D R field simulation with light to dark representing large to small radii. The simulation used unit locations from Figure 1a and cumulative probability distribution functions for R built from drainage curves measured on each unit. (c) Comparison of measured and simulated drainage curves for each unit. Triangles denote the fine sand, squares denote the medium sand, and circles denote the coarse sand (solid lines designate data and dashed lines designate simulations).

Table 3. Invaded Nonwetting Volume at Breakthrough

		Notes	Volume, ^a mL
		<i>CO</i> ₂	
Experiment	from GCP		50.8
NP MMIP	initial		60.2 ± 0.7
NP MMIP	modified <i>R</i> field (e.g., Plates 2a and 3b)		51.3 ± 0.5
		<i>TCE</i>	
Experiment	from GCP		73.1
NP MMIP	initial		53.1 ± 0.9
NP MMIP	modified <i>R</i> field (e.g., Plate 2b)		40.3 ± 0.4
NP MMIP	modified <i>R</i> field, viscous 1 block/step (e.g., Plate 2c)		64.8 ± 0.5
NP MMIP	modified <i>R</i> field, viscous 10 blocks/step		66.0 ± 0.5
NP MMIP	modified <i>R</i> field, viscous 20 blocks/step		67.3 ± 0.5
NP MMIP	modified <i>R</i> field, viscous 30 blocks/step		68.7 ± 0.5
NP MMIP	modified <i>R</i> field, viscous 40 blocks/step		70.1 ± 0.5
NP MMIP	modified <i>R</i> field, viscous 50 blocks/step		71.5 ± 0.5
NP MMIP	modified <i>R</i> field, viscous 60 blocks/step (e.g., Plates 2d and 3d)		72.9 ± 0.5

^aStandard deviation is associated with variation over 10 realizations.

ever, we see many quantitative differences between simulations and experiment, for example, pool height and finger width, which lead to significant errors in the total volume invaded at breakthrough (see Table 3). Colors in Plate 1 represent invasion order, and when they match between images, the sequence in time matches as well. Most of the volume and invasion sequence error is found associated with the pools. Additionally, comparison of TCE to CO₂ simulations shows the TCE invasion pathway to have pools of lower height and connecting fingers that are slightly narrower, exactly opposite of what we found experimentally.

There are two main causes for the discrepancies between our initial simulations and experiments. First, there is a mismatch between the capillary properties measured for the medium sand units and those composing the CB units within the heterogeneous sand slab. This causes pool height above CBs for CO₂ invasion to be overpredicted by ~25%. We also see a slight mismatch of capillary properties at the narrowest point of the coarse sand run in the middle of the chamber. Here two units of the medium sand came very near to each other, and close inspection showed that some of the medium sand mixed with the coarse thus reducing the local *R* values at the restriction point. The second cause is the neglect of viscous forces in our model formulation (i.e., equation (3)). Our simulations yield pool heights above CBs that are lower for TCE than for CO₂ and finger widths that are slightly narrower, consistent with an assumption of negligible viscous forces. However, as GCP showed, viscous forces are not negligible for the TCE invasions, and so experimental pool height and finger width is actually greater for TCE than CO₂. Additionally, the breaching of CBs occurs at only a single point, while we found multiple fingers to span the CB for TCE, also an influence of increased viscous forces. To better simulate the experiments, we now consider several modifications that address these property and viscous discrepancies.

3.3. *R* Field Modifications

The increase in the pore sizes within the medium sand CBs is easily captured by scaling its *R* distribution. When viscous forces are negligible, the analysis of GCP found a factor of 1.1 was required to fit the experimental pool heights for the CO₂ invasion. In order to capture the additional influence of the

coarse and medium sand mixing at the restriction within the long coarse sand run in the middle of the chamber, we also scaled the *R* in this region by a factor of 0.95. Results shown in Plate 2a show that we now simulate pool heights very well for CO₂ including that above the middle restriction. Additionally, the invasion order is now nearly identical to the experiment as is the CO₂ volume at breakthrough (see Table 3). For TCE, shown in Plate 2b, pool height is further depressed with correspondingly greater discrepancies for invasion order and TCE volume.

3.4. Viscous Force Modifications

To fully treat the TCE invasion, we must include viscous forces within the NP MMIP model. Two approaches have been suggested recently in the literature. *Xu et al.* [1998] consider a viscous influence proportional to the capillary number and viscosity ratio. *Ewing and Berkowitz* [1998] make use of two statistical relations that modify the IP search algorithm to first

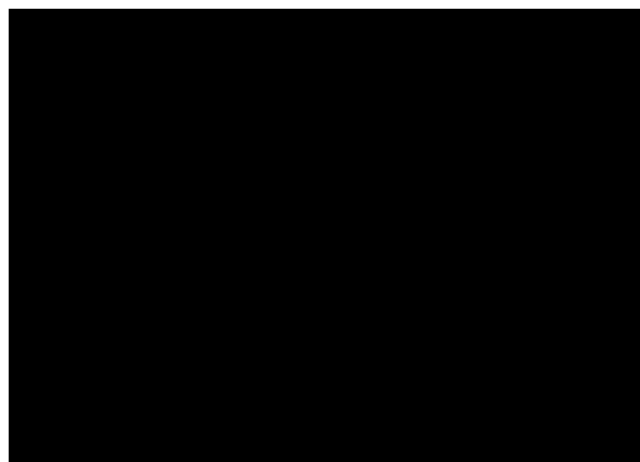


Figure 2. Magnified and contrast-enhanced CO₂ saturation structures below CB4: (a) CO₂ experiment and (b) NP MMIP simulation on the scaled *R* field. Saturation fields have been contrast enhanced to bring out the underlying pore-scale nature of fingers in the thickness-integrated fields. The box shows a representative CO₂ finger width of 0.7 cm.

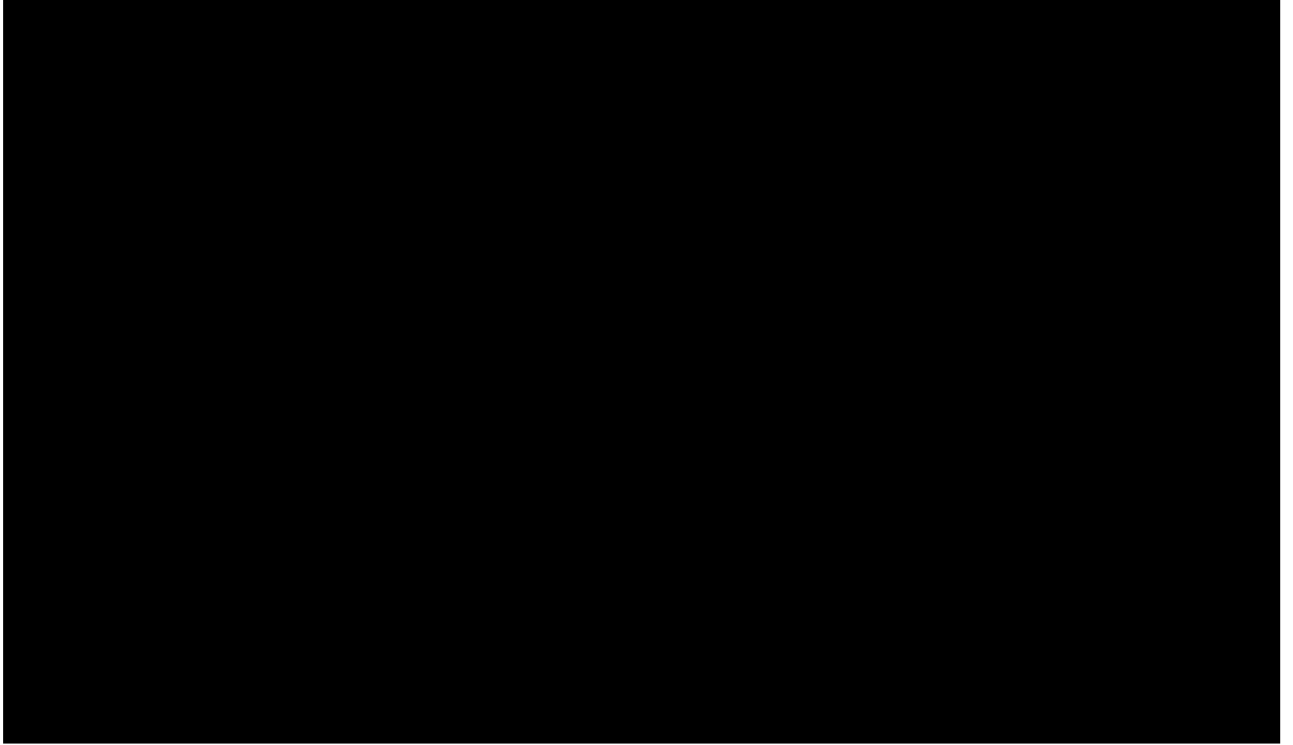


Figure 3. Magnified and contrast-enhanced TCE saturation structures below CB4: (a) TCE experiment and NP MMIP simulations on the scaled R field with first- and second-order viscous effect with (b) 1, (c) 10, (d) 20, (e) 30, (f) 40, (g) 50, and (h) 60 blocks per step. Saturation fields have been contrast enhanced to bring out the underlying pore-scale nature of fingers in the thickness-integrated fields. The box shows a representative TCE finger width of 1.2 cm.

cause the filling in of the network behind the front and, second, to initiate independent gravity-driven fingers. While each of these approaches is instructive, neither is able to fully explain the experimental behavior of GCP. Here we propose an alternative approach that includes first-order viscous effects similar to *Xu et al.* [1998] and then second-order effects similar to *Ewing and Berkowitz* [1998]. We have defined the order operationally with respect to the influence on the total volume invaded in our experiments and note that, depending on the system heterogeneity, the order may be reversed. For each of these our formulations are guided by data and depart somewhat from the previous theoretical development.

On the basis of experimental results, GCP found that in every case considered (e.g., finger width, finger pulsation, maximum pool height, and pool pulsation), incorporating viscous forces within the invading phase alone with appropriate recognition of the conducting pore-scale geometry allowed us to predict experimental behavior, i.e., pool height and finger width, closely. Viscous forces increase the pressure within the invading phase from the invading front back to the source. Assuming the defending phase's pressure is uninfluenced, the P_t required to span a block decreases back along this path as well. Thus we propose the total block spanning pressure can be modified to include first-order viscous forces as

$$P_t = \frac{-2\sigma \cos(\alpha)}{R} + \Delta\rho g z - \frac{Q\mu L}{kA}, \quad (4)$$

where Q is the applied flow rate, μ is the viscosity of the invading fluid, L is the distance back along the flow path from the invasion front to the block of interest, k is the permeability

of the phase structure along the path, and A is the cross-sectional area of the conducting pathway normal to the local flux. Generally, k and A will vary along L and in time as invasion proceeds and will vary with Q if the applied flow varies in time. As discussed by GCP, for fingers, A corresponds to the conductive finger backbone, while within the pools, A increases to the full cross-sectional area normal to the flow direction as the pool fills. Full implementation of (4) requires that A , L , and k be determined locally as the invasion progresses, a complicated and computationally expensive task outside the scope of this paper. Here we are interested in a simplified effective application that is accomplished within the context of the current NP MMIP model. Therefore we focus on the critical situations in the experiment where viscous forces are nonnegligible and incorporate them in an effective sense thus avoiding local transient modification of P_t .

Our primary viscous discrepancy occurs at CBs where viscous forces primarily act vertically. For this one dimensional view, $L = z_f - z$, where z_f is the position of the front. Taking effective values for k and A (both with subscript e) that apply to the pool/CB system, we may write

$$P_t = \frac{-2\sigma \cos(\alpha)}{R} + \left[\Delta\rho g + \frac{Q\mu}{k_e A_e} \right] z - \frac{Q\mu}{k_e A_e} z_f. \quad (5)$$

Recognizing that the final term is a constant throughout the invading phase at a given growth step, it does not influence the choice of which block to invade. Thus, in this first order formulation we see that the viscous term simply adds to the gravitational term and can be incorporated globally within NP MMIP. For the gravity-destabilized flows we consider here, the

intrinsically positive viscous term diminishes the influence of gravity. To approximate the effective viscous factor, we consider the increase in pool height above CBs. Using the relation for the maximum pool height developed in the scale analysis of GCP (i.e., their (5)), simplifying it to an effective system composed of a pool and barrier with single effective k and A , denoting the value of the pool height with no viscous influence as h_{pcap} and that with viscous influence as h_{pvis} , and solving for the viscous factor yields

$$\frac{Q\mu}{k_e A_e} \sim \Delta\rho g \left[\frac{h_{\text{pcap}}}{h_{\text{pvis}}} - 1 \right]. \quad (6)$$

Note (6) has been written to be positive in context of our current problem and definitions. The ratio of h_{pcap} to h_{pvis} for the medium-coarse sand CB in the TCE experiments was found to be 0.52. Applying (5) globally using this viscous factor will also slightly increase vertical finger width. It will not, however, influence horizontal paths. Nonnegligible viscous forces along a primarily horizontal path are inferred experimentally within the pool above CB4 where the pool is higher near the entry point on the right than on the far left. We can treat this discrepancy regionally by including a horizontal component of the viscous pressure using the measured value of the intrinsic permeability as k for the coarse unit and taking A_e to be the height of the pool. A simulation on the modified R distribution field that includes both the global vertical viscous component and the horizontal component in this pool is shown in Plate 2c. We now capture quite well both the maximum height and lateral extent of the TCE pool above CB4 as well as the invasion order. Additionally, total TCE volume at breakthrough is now within $\sim 10\%$ of the experimental value (see Table 3).

In comparison to experiment, while the simulated TCE fingers widen slightly by use of (5), they are still too narrow, and their multiple and braided nature is not well represented. In the work of GCP, this second-order viscous effect caused TCE finger saturation to increase well above that for CO_2 signifying an increase in the range of pore sizes that fill. At the “front” where the relative permeability increases from zero, the influence of the randomness in the capillary pressure relative to the pressure drop due to viscous forces decreases as Q increases. Physically, the system cannot distinguish between blocks when their capillary pressures are within a certain range of each other, and so the spread of R selected should widen, and local saturation should increase. Thus, in NP MMIP the range of P_t that is filled at each growth step should also increase as Q increases. This effect is similar to that emphasized in the work of *Ewing and Berkowitz* [1998], where they consider a random selection of a single pore within the range to be filled. In our conceptualization we would simply fill all the pores within the range that are accessible at a given growth step. In this sense, we consider viscous forces to decrease the randomness imposed by capillary forces at the front. While a relationship between the range of P_t to be filled as a function of Q requires further study to properly parameterize, we include this effect only roughly in the current model by assuming that this range is correlated to a set number of blocks at the top of the sorted P_t list; the larger the range is, the larger this number of blocks is. In our implementation we then simply fill a set number of blocks at the top of the sorted P_t list at each growth step (instead of a single block) before resorting the list.

A TCE order image is shown in Plate 2d for a choice of blocks filled per growth step (60) that best matches the total volume of TCE at breakthrough. The braided nature of the

growth structure as seen within each capillary barrier and within the coarse sand unit between CB3 and CB4 is reasonably well simulated. However, the multiple, independent finger formation seen in the experiment below CB4 is not strong. While two fingers formed below the CB in the simulation, they do not remain independent, the one on the left stalled while the one on the right continued growing. Across the 10 simulations this was the only one to yield such distinct paths through the CB. This third-order viscous effect may require full implementation of (4) or the imposition of an additional independency criterion such as suggested by *Ewing and Berkowitz* [1998]. However, we note that multiple fingers also form in the CO_2 experiment because of pulsation even though viscous forces were negligible (see bottom of Plate 1a), and so the cause of independent fingers and thus their appropriate modeling is as yet unclear.

3.5. Saturation Fields for Modified Simulations

Saturation fields for the experimental and final modified CO_2 and TCE NP MMIP results are shown in Plate 3. As mentioned by GCP, we have local error in the experimental saturation fields due to blurring around the edges of units and fingers. Because of this and the fact that we did not have a fully TCE saturated image to reduce the TCE data, the total volume in the experimental saturation image is underpredicted by $\sim 8\%$ for CO_2 , while that for TCE is overpredicted by $\sim 12\%$. Considering these errors, simulations and experiments appear very close. Average values of saturation within the center of pools where we have the least measurement error are within 1–2%. Saturations within CBs for TCE appear to be slightly underpredicted; however, we have the most experimental error in these locations of unit transition. Additionally, we note that use of an effective viscous correction such as (5) will slightly underemphasize local viscous effects in the CB and thus should somewhat underpredict the multiple and braided nature there, while slightly overpredicting it in the coarse layer. The simulated CO_2 and TCE saturation structures within the coarse sand between CB3 and CB4 are very similar to the experiment. This is also the case for the fingers below CB4.

Figures 2 and 3 show magnified and contrast-enhanced images of the saturation fields at and below CB4. A series of simulations for increasing blocks per step is included for TCE in Figure 3. In all the images we see the beginnings of several fingers extending into the CB. For CO_2 both experiment and simulation show one finger to extend through the CB and grow below. For TCE, three fingers extend fully through the barrier in the experiment, while two do so in the simulation. Multiple breaches occur for TCE in both simulations and experiment at all of the other CBs as well. Average finger widths below CB4 are very close for the CO_2 , while for the TCE the simulated width at 60 blocks per step where the total volume at breakthrough is matched is closer to the combined width of all the fingers in the experiment. The finger width for 10 blocks per step better simulates the experimental width for an individual TCE finger. Obviously, if the IP algorithm is modified to allow independent fingers, Q for each would have to be determined and the appropriate range of P_t to be filled (e.g., number of blocks per step in our rough implementation) would have to be specified.

It is important to realize that working to simulate the finger structure better in our macroheterogeneous media such as considered here is not very important by itself in the simulation of the total volume invaded. Note that if the second-order

viscous modification that allows us to predict the multiple and braided finger structure in the TCE experiment is neglected, we are still within $\sim 10\%$ on the invaded volume (see Plate 1c and Table 3). It is clear that in order to reasonably predict the volume invaded, it is most important to properly predict pool heights, and it is in this context that fingers have a first-order influence. Adequate recognition of the finger structure within a CB must be made to elevate the pool heights in the TCE experiments and yield the corresponding increase of $\sim 180\%$ in the total volume invaded.

Finally, we note that in our current presentation, the simultaneous invasion of wetting and nonwetting fluid has not been considered, and so pulsation is not simulated; we model a static invasion structure that is of maximum extent and saturation. Pulsation occurs throughout the CO_2 and parts of the TCE experiment; however, as we see here, it does not significantly influence the path in our particular macroheterogeneous porous media nor the adequate prediction of the total invaded volume at breakthrough. For less intense heterogeneities, however, this may not be the case as is exemplified for the CO_2 below CB4 where the single finger breaks into several with depth.

4. Summary and Concluding Remarks

In the context of macromodified invasion percolation (MMIP) we reconceptualize at the near pore (NP) scale and apply the model to simulate the nonwetting phase invasion experiments of GCP conducted in macroheterogeneous porous media. NP MMIP shows the same characteristic alternation as found experimentally between gravity-stabilized and destabilized invasion growth controlled by the presence of CBs. The breaching of these barriers and subsequent pore-scale fingering of the nonwetting phase is represented extremely well by NP MMIP. For the CO_2 experiment where viscous forces were negligible, slight modifications of the capillary properties (also suggested by the scale analysis of GCP) were required to fully match the experimental pool heights, after which the total volume invaded matched experimental measurements. However, for the TCE experiment with a viscosity ~ 40 times that of CO_2 , considerable discrepancies remained.

In order to consider situations where viscous forces are nonnegligible, we redefined the total pore-filling pressure to include viscous losses within the invading phase as well as its influence to decrease the randomness imposed by capillary forces at the front. Our simulations that include these viscous influences in an effective sense are shown to match experiments very well. However, full implementation of viscous forces using (4) requires a more complete understanding of the role of viscous forces at the pore scale as the invasion process evolves. In particular, two general relationships must be built that model (1) the number of conducting backbone pores within the invading structure in time and space and (2) the indistinguishability between blocks at the front. Each of these relationships must be determined as a function of the flow rate. We show a good match to experiments when we can back calculate the appropriate values; however, currently these are little more than empirical "dials" that allow for calibration. Further research is required to theoretically and experimentally develop these general relationships.

While our current results represent a significant step, much beyond viscous influences remains to be considered to build a solid foundation for MMIP models. Research is required to

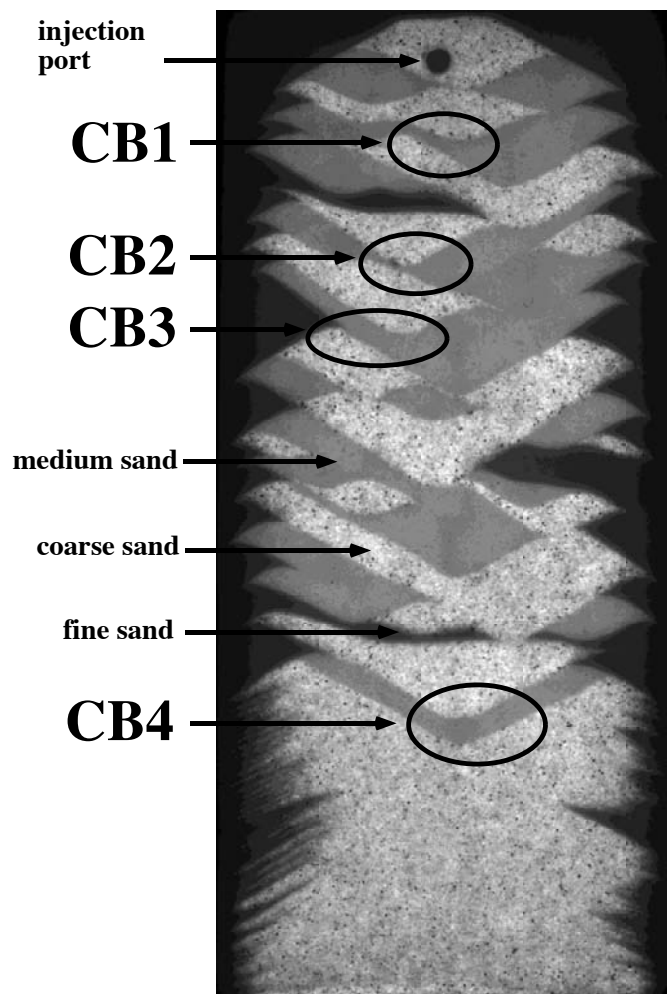
consider fully the influences of (1) capillary, gravity, and viscous forces on length scales for finger diameter and pool height at capillary barriers; (2) pore size distribution and subscale heterogeneities on the definition and scaling of R ; and (3) simultaneous wetting and nonwetting fluid invasion that yields subsequent pulsation on the generation of independent pathways within a heterogeneous formation. Additionally, many implementation issues remain to be fully evaluated such as the choice of optimal connectivities for the network domain. With these accomplished, the application of forms of MMIP to field-scale problems where subscale lengths are assembled to yield the nonwetting phase migration pathway directly may then be possible.

Acknowledgments. This research was partially supported by Sandia National Laboratory's Research and Development Program, the U.S. Department of Energy's Environmental Science Management Program, and the U.S. Department of Energy's Basic Energy Science Geoscience Program under contract DE-AC04-94AL85000. We thank Will Peplinski for reducing the experimental heterostructure to the unit image used to create the realization for the R fields. The initial simulations in this paper were first presented by the senior author at the American Geophysical Union 1995 Fall Meeting [Conrad *et al.*, 1995], and conversations at that time with Toby Ewing, Brian Berkowitz, and Harvey Scher are gratefully acknowledged. Finally, we thank Toby Ewing, Clinton Willson, and an anonymous reviewer for their constructive criticism of the manuscript.

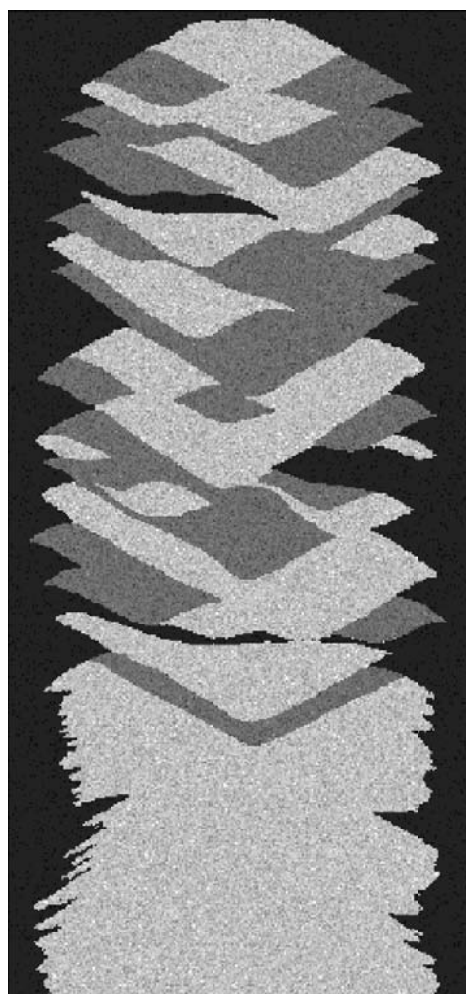
References

- Conrad, S. H., R. J. Glass, W. Peplinski, L. Yarrington, and E. K. Webb, Nonaqueous phase liquid movement within heterogeneous porous media: Physical experiment and numerical simulation (abstract), *Eos Trans. AGU*, 76(46), Fall Meet. Suppl., F258, 1995.
- Ewing, R. P., and B. Berkowitz, A generalized model for simulating initial migration of dense non-aqueous phase liquids, *Water Resour. Res.*, 34(4), 611–622, 1998.
- Glass, R. J., S. H. Conrad, and E. K. Webb, Percolation approaches to modeling immiscible fluid movement in subsurface systems (abstract), *Eos Trans. AGU*, 74(43), Fall Meet. Suppl., 278, 1993.
- Glass, R. J., E. K. Webb, and S. H. Conrad, An upscaled buoyant invasion percolation model for use in approaches to delineate subsurface DNAPL location, *AICHE Symp. Ser.*, 306(91), 23–29, 1995.
- Glass, R. J., S. H. Conrad, and W. Peplinski, Gravity-destabilized nonwetting phase invasion in macroheterogeneous porous media: Experimental observations of invasion dynamics and scale analysis, *Water Resour. Res.*, 36(11), 3121–3137, 2000.
- Ioannidis, M. A., I. Chatzis, and F. A. L. Dullien, Macroscopic percolation model of immiscible displacement: Effects of buoyancy and spatial structure, *Water Resour. Res.*, 32(11), 3297–3310, 1996.
- Kueper, B. H., and D. B. McWhorter, The use of macroscopic percolation theory to construct large-scale capillary pressure curves, *Water Resour. Res.*, 28(9), 2425–2436, 1992.
- Lenormand, R., and C. Zarcone, Invasion percolation in an etched network: Measurement of a fractal dimension, *Phys. Rev. Lett.*, 54, 2226–2229, 1985.
- Reeves, P. C., and M. A. Celia, A functional relationship between capillary pressure, saturation and interfacial area as revealed by a pore-scale network model, *Water Resour. Res.*, 32(5), 2345–2358, 1996.
- Wilkinson, D., and J. F. Willemsen, Invasion percolation: A new form of percolation theory, *J. Phys. A Math. Gen.*, 16, 3365–3376, 1983.
- Xu, B., Y. C. Yortsos, and D. Salin, Invasion percolation with viscous forces, *Phys. Rev. E Stat. Phys. Plasmas Fluids Relat. Interdiscip. Top.*, 57(1), 739–751, 1998.
- S. H. Conrad, R. J. Glass, and L. Yarrington, Flow Visualization and Processes Laboratory, Sandia National Laboratories, P.O. Box 5800, Albuquerque, NM 87185-0735. (shconra@sandia.gov; rjglass@sandia.gov; lyarrin@sandia.gov)

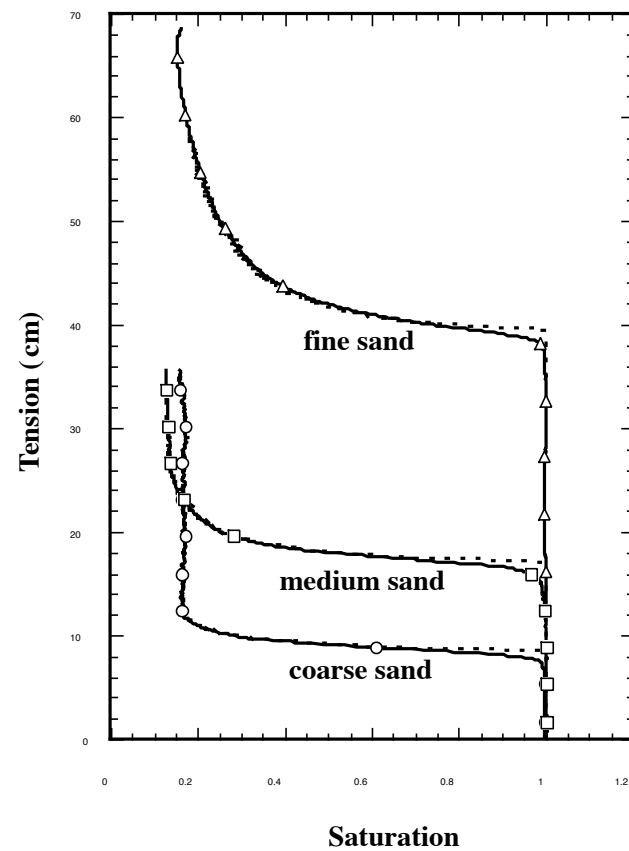
(Received November 19, 1999; revised July 11, 2000; accepted September 15, 2000.)



a) Experimental hetero-structure



b) Representative R field simulation



c) Drainage curve data and simulation

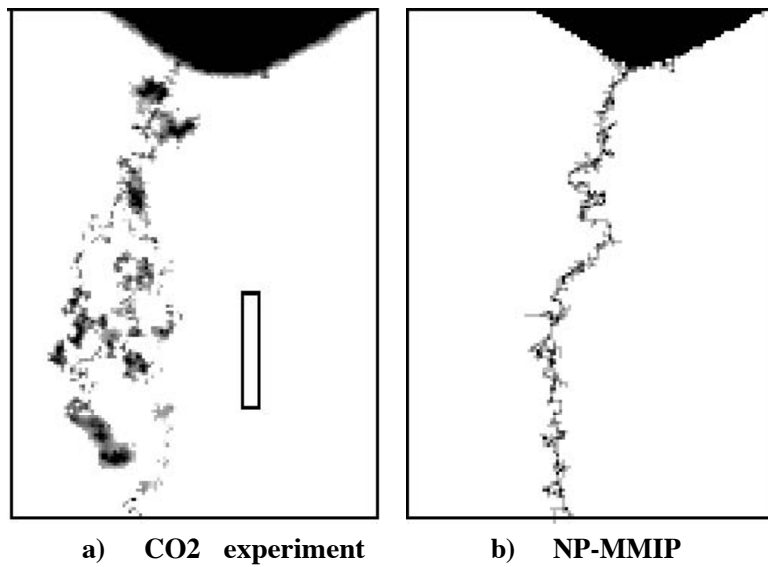


Figure 2. Magnified and contrast enhanced CO₂ saturation structures below CB4: a) CO₂ experiment, b) NP-MMIP simulation on the scaled R field. Saturation fields have been contrast enhanced to bring out the underlying pore scale nature of fingers in the thickness integrated fields. The box shows a representative CO₂ finger width of 0.7 cm

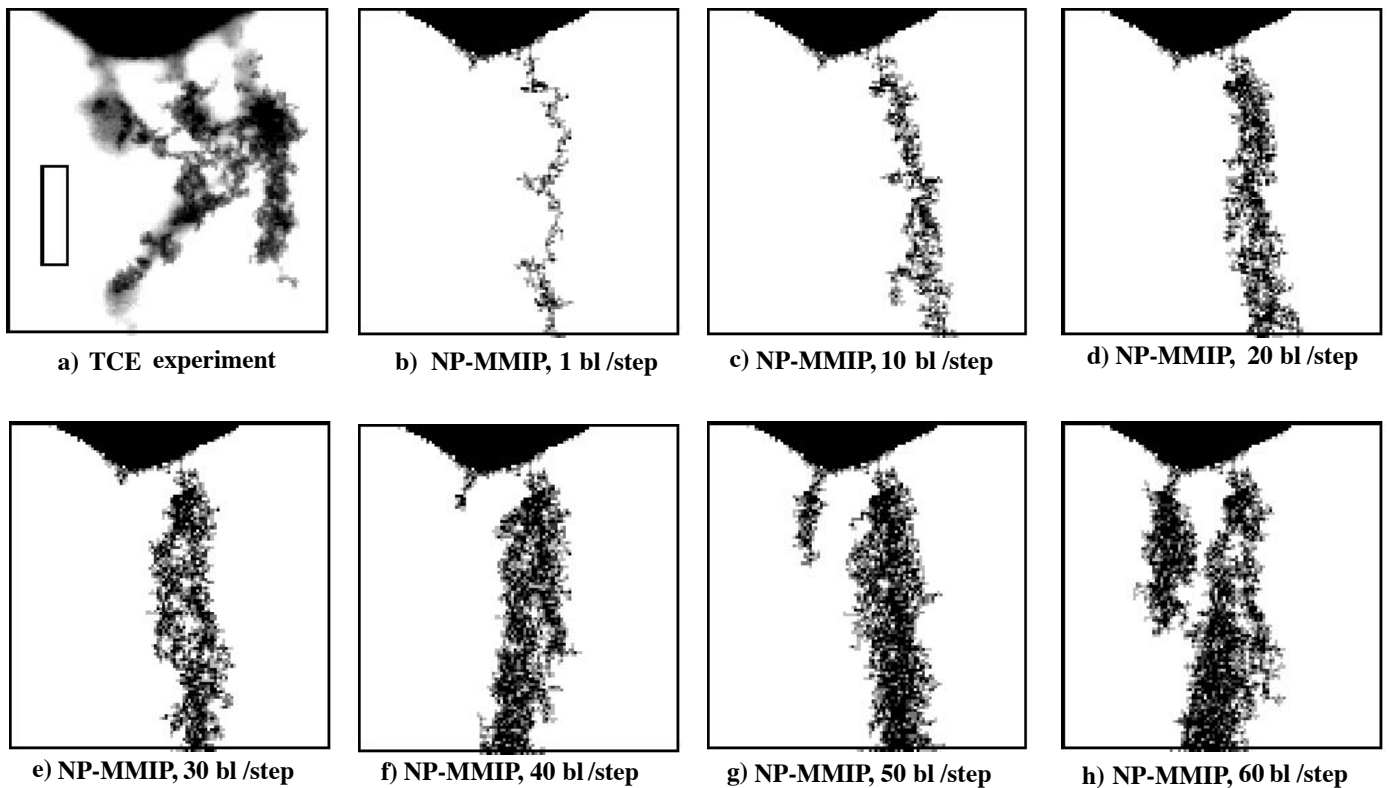


Figure 3. Magnified and contrast enhanced TCE saturation structures below CB4: a) TCE experiment, and NP-MMIP simulations on the scaled R field with first and second order viscous effect with b) 1, c) 10, d) 20, e) 30, f) 40, g) 50, and h) 60 blocks per step. Saturation fields have been contrast enhanced to bring out the underlying pore scale nature of fingers in the thickness integrated fields. The box shows a representative TCE finger width of 1.2 cm.